



# Pseudocolor enhancement of mammogram texture abnormalities

Michal Haindl<sup>1</sup> · Václav Remeš<sup>1</sup>

Received: 11 January 2018 / Revised: 14 December 2018 / Accepted: 1 April 2019 / Published online: 15 April 2019  
© Springer-Verlag GmbH Germany, part of Springer Nature 2019

## Abstract

We present a novel method for enhancing texture irregularities, both lesions and microcalcifications, in digital X-ray mammograms. It can be implemented in computer-aided diagnostic systems to help improve radiologists' diagnosis precision. The method provides three different outputs aimed at enhancing three different sizes of mammogram abnormalities. Our approach uses a two-dimensional adaptive causal autoregressive texture model to represent local texture characteristics. Based on these, we enhance suspicious breast tissue abnormalities, such as microcalcifications and masses, to make signs of developing cancer better visually discernible. We extract over 200 local textural features from different frequency bands, which are then combined into a single multichannel image using the Karhunen–Loeve transform. We propose an extension to existing contrast measures for the evaluation of contrast around regions of interest. Our method was extensively tested on the INbreast database and compared both visually and numerically with three state-of-the-art enhancement methods, with favorable results.

**Keywords** Mammograms · Region of interest enhancement · Computer-aided diagnosis · Texture model · Markov random field

**Mathematics Subject Classification** 60J25 · 60G60 · 62M40 · 68U10 · 62P10

## 1 Introduction

Breast cancer is the most common type of cancer among middle-aged women in most developed countries [14,22]. Up to 10% of women have breast cancer during their lives. Developed countries try to fight this increasingly dangerous trend by encouraging women to attend preventive mammography screenings regularly. Unfortunately, around one in four radiologically visible cancers is missed during the screenings [20], resulting in millions of cancer cases being overlooked. Therefore, many lives could be saved by even the slightest improvement in the detection methods. However, radiologists tend to consider current CAD (computer-aided diagnosis) methods to be misleading since even though there are only about eight malignant mammograms in 1000 [20], 2–3 regions of interest (ROIs) per mammogram on average

are pointed out by most CAD systems (e.g., [8,22]). Thus, CAD results in 250–370 false positives per one true malignant case.

To assist the radiologists with the visual evaluation of mammograms, automatic enhancement of the mammograms is a popular alternative to CAD classification. Several mammogram enhancement methods have been published, e.g., [1–3,5,11,13,16,17,19,21,23,24]. Dippel et al. [3] compare the merits of using either Laplacian pyramids or wavelet analysis for whole-mammogram enhancement, Mencattini et al. [11] selectively enhance segmented mammogram regions using wavelet transformation, Sakellaropoulos et al. [16] design an adaptive wavelet-based method for enhancing the contrast of entire mammograms, and Salvado and Roque [17] use wavelet analysis to detect microcalcifications.

Mammogram texture representation based on a local statistical Gaussian mixture was used in [5] to evaluate screening mammograms. This method estimates the multivariate probability density of pixel values within a floating window around the central pixel using the Gaussian mixture model. The enhancement is then based on the log-likelihoods computed for each pixel. Since abnormalities have a low probability of occurrence, they are marked as areas with the

✉ Michal Haindl  
haindl@utia.cas.cz  
Václav Remeš  
remes@utia.cas.cz

<sup>1</sup> Department of Pattern Recognition, Institute of Information Theory and Automation, Czech Academy of Sciences, Pod Vodárenskou věží 4, Prague, Czech Republic

lowest log-likelihood. The method is, however, computationally very demanding.

The novelty of our method lies in selectively highlighting textural abnormalities while lowering the contrast of the benign rest of the image, and the use of several frequency bands and different specifically targeted statistics combined in the multichannel output. The color-coded, additionally computed image statistics undoubtedly present more information than grayscale images. Another novel feature of our method is the use of multiple frequency bands sensitive to different sizes of abnormalities.

For modeling breast tissue texture, we use the two-dimensional adaptive causal autoregressive texture model (2DCAR) [7,10], which is very fast and efficient to compute.

## 2 Material and methods

### 2.1 Predictive textural model

The mammography tissue textures in the form of mono-spectral images are locally modeled by their dedicated directional Gaussian noise-driven autoregressive random-field two-dimensional model, because this model has good modeling performance; i.e., it can even be used for mammographic tissue texture synthesis. At the same time, this model is high speed and allows for analytical treatment of all relevant statistics [6,7]. 2DCAR is a random field of the Markovian type. It has the joint conditional probability density on the set of all possible realizations  $Y$  of the  $M \times N$  lattice  $I$

$$p(Y | \gamma_\phi, \sigma_\phi^{-2}) = (2\pi\sigma_\phi^2)^{-\frac{MN-1}{2}} \exp \left\{ \frac{-1}{2} tr \left\{ \sigma_\phi^{-2} \begin{pmatrix} -\alpha \\ \gamma_\phi^T \end{pmatrix}^T \tilde{V}_{MN-1} \begin{pmatrix} -\alpha \\ \gamma_\phi^T \end{pmatrix} \right\} \right\}, \tag{1}$$

where  $tr()$  is the trace of the corresponding matrix,  $\alpha$  is a unit vector and the following notation is used:

$$\tilde{V}_{r-1} = \sum_{k=1}^{r-1} \begin{pmatrix} Y_k Y_k^T & Y_k X_k^T \\ X_k Y_k^T & X_k X_k^T \end{pmatrix} = \begin{pmatrix} \tilde{V}_{y(r-1)} & \tilde{V}_{xy(r-1)}^T \\ \tilde{V}_{xy(r-1)} & \tilde{V}_{x(r-1)} \end{pmatrix}. \tag{2}$$

Here,  $r = [r_1, r_2, \phi]$  is a spatial multi-index denoting history of movements on the rectangular lattice  $I$ , where  $r_1, r_2$  are row and column indices, and

$$\phi \in \{0^\circ, 45^\circ, 90^\circ, 135^\circ, 180^\circ, 225^\circ, 270^\circ, 315^\circ\} \tag{3}$$

is the direction of the model development. The 2DCAR model can be expressed as a stationary causal uncorrelated noise-driven 2D autoregressive process:

$$Y_r = \gamma_\phi X_r + e_r, \tag{4}$$

where  $\gamma_\phi$  is the  $1 \times \eta$  parameter vector and  $\eta$  is the cardinality of the causal (or alternatively unilateral) contextual neighborhood  $I_r^c$  (i.e., all the support pixels were previously visited, and thus their values are known). Furthermore,  $e_r$  denotes white Gaussian noise with zero mean and a constant but unknown variance  $\sigma^2$ , and  $X_r$  is a support vector of  $Y_{r-s}$  where  $s \in I_r^c$ . The method uses a locally adaptive version of this 2DCAR model [7], where its recursive statistics are modified by an exponential forgetting factor, i.e., a constant smaller than one which is used to weight the older data.

### Parameter estimation

Parameter estimation of the 2DCAR model using the maximum likelihood, least-square or Bayesian methods can be resolved analytically. The Bayesian parameter estimates in the 2DCAR model using the normal-gamma parameter prior are:

$$\hat{\gamma}_{r-1}^T = V_{x(r-1)}^{-1} V_{xy(r-1)}, \tag{5}$$

$$\hat{\sigma}_{r-1}^2 = \frac{\lambda_{(r-1)}}{\beta(r)}, \tag{6}$$

where

$$\lambda_{(r-1)} = V_{y(r-1)} - V_{xy(r-1)}^T V_{x(r-1)}^{-1} V_{xy(r-1)}, \tag{7}$$

$$V_{(r-1)} = \tilde{V}_{(r-1)} + V_{(0)}, \tag{8}$$

$$\beta(r) = \beta(0) + r - 1, \tag{9}$$

$\beta(0)$  is an initialization constant, and submatrices in  $V_{(0)}$  come from the parameter's prior distribution. For our purposes, we set  $\beta(0) = \eta - 1$  and  $V_{(0)}$  (8) to the unit matrix. Parameter estimates (5) and (6) can also be evaluated recursively [7]. The posterior probability density [7] of the model is:

$$p(Y_r | Y^{(r-1)}) = \frac{\Gamma\left(\frac{\beta(r)-\eta+3}{2}\right)}{\Gamma\left(\frac{\beta(r)-\eta+2}{2}\right) \pi^{\frac{1}{2}} \left(1 + X_r^T V_{x(r-1)}^{-1} X_r\right)^{\frac{1}{2}} |\lambda_{(r-1)}|^{\frac{1}{2}}} \left(1 + \frac{(Y_r - \hat{\gamma}_{r-1} X_r)^T \lambda_{(r-1)}^{-1} (Y_r - \hat{\gamma}_{r-1} X_r)}{1 + X_r^T V_{x(r-1)}^{-1} X_r}\right)^{-\frac{\beta(r)-\eta+3}{2}}. \tag{10}$$

The conditional mean value predictor of the one-step-ahead predictive posterior density (10) for the normal-gamma parameter prior is

$$E \left\{ Y_r | Y^{(r-1)} \right\} = \hat{\gamma}_{r-1} X_r. \tag{11}$$

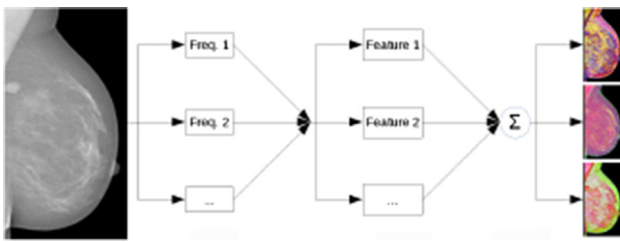


Fig. 1 Enhancement method’s flowchart

## 2.2 Proposed pseudocolor enhancement

The mammogram enhancement is based on the efficient computation of several hundred textural statistics, their subsequent decorrelation and visualization of a weighted combination of the three most informative transformed features and the original X-ray mammogram. Figure 1 shows the flowchart of the method, which is described in more detail in the following text.

To compute the mammogram enhancement features, the following statistics are evaluated for each pixel in the original mammogram measurements for all directions, as well as in the smoothed variants obtained by median filters with window sizes 2, 3, 5, 8 and 10:

### 2.2.1 Prediction error

The prediction error, based on Eq. (11), can be computed as

$$Err_{\text{pred}}^r = E \left\{ Y_r | Y^{(r-1)} \right\} - Y_r. \tag{12}$$

This statistic is sensitive to smaller- to medium-sized texture abnormalities, such as lymph nodes.

### 2.2.2 Absolute value of the prediction error

The absolute value of the previously defined (12) prediction error is

$$|Err_{\text{pred}}^r| = \left| E \left\{ Y_r | Y^{(r-1)} \right\} - Y_r \right|. \tag{13}$$

This statistic is sensitive to small texture abnormalities such as lymph nodes, necrotic calcification and larger benign calcifications.

### 2.2.3 Innovation error

The innovation error is based on Eq. (11), and this statistic combines the prediction error with the gradient:

$$Err_{\text{in}}^r = E \left\{ Y_{r-1} | Y^{(r-2)} \right\} - Y_r. \tag{14}$$

The innovation error highlights very small texture abnormalities with sharp edges.

### 2.2.4 Absolute value of the innovation error

The absolute value of the innovation error is

$$|Err_{\text{in}}^r| = \left| E \left\{ Y_{r-1} | Y^{(r-2)} \right\} - Y_r \right|. \tag{15}$$

This statistic is sensitive to very small texture abnormalities, such as microcalcifications.

### 2.2.5 Prediction probability

The prediction probability is Eq. (10). This statistic is sensitive to medium-sized and larger texture abnormalities, such as lesions and larger lymph nodes.

This way we get new images corresponding to the original mammogram but emphasizing its different texture features. Because the 2DCAR model is directionally dependent, each analysis is also performed separately for each of the eight different basic directions  $\phi$  (3).

The resulting model statistics (10) and (12) through (15) are stored in 240 planes (five different statistics (10), (12), (13), (14) and (15) computed on the original and five median filtered images for eight directions  $\phi$  (3)) with the same dimensions as the original image. These 240 computed features have various spatially dependent mutual correlations. The Karhunen–Loeve transform is then performed on these planes in order to obtain the most informatively transformed three components (99% of the overall eigenvalues), which are then assigned, respectively, to the red, green and blue color channels of the resulting enhanced image. The latter thus consists of the original X-ray measurement and a linear combination of the computed textural statistics. Different partial results are susceptible to different-sized abnormalities; in particular, the prediction error components are better for enhancement of smaller findings, such as microcalcifications. The analysis based on prediction probability is, on the other hand, more susceptible to more substantial abnormalities, such as lesions and masses.

Our method produces three different outputs (enhanced pseudocolor images) targeted to three distinct mammogram abnormalities (larger spots, microcalcifications and combined but with slightly compromised contrast):

1. Based purely on prediction probability (Sect. 2.2.5) (16): These results tend to be smoother and work very well on larger areas, e.g., in Fig. 3—top row, second image.
2. Based purely on prediction errors (Sects. 2.2.1, 2.2.2) (17): good enhancement of smaller abnormalities such as microcalcifications, e.g., in Fig. 5—top row, third image.

3. All aspects combined (Sects. 2.2.1, 2.2.2, 2.2.3, 2.2.4 and 2.2.5) (18): joins the advantages of both of the previous methods, but does not have such good contrast, e.g., in Fig. 4—top row, fourth image.

$$\mathbb{Y}_r^b = T_b \left( p(Y_r | Y^{(r-1)}), \dots \right)^T, \quad (16)$$

$$\mathbb{Y}_r^s = T_s \left( Err_{pred}^r, |Err_{pred}^r|, Err_{in}^r, |Err_{in}^r|, \dots \right)^T, \quad (17)$$

$$\mathbb{Y}_r^m = T_m \left( Err_{pred}^r, |Err_{pred}^r|, Err_{in}^r, |Err_{in}^r|, p(Y_r | Y^{(r-1)}), \dots \right)^T, \quad (18)$$

where  $T$  are  $3 \times \{48, 192, 240\}$  transformation matrices. Matrix rows are eigenvectors corresponding to the three largest eigenvalues from the actual data spaces.

Finally, the enhanced mammograms are optionally combined with the original image to enable the radiologist to perceive both the enhancement and the original structure of the breast and customize the ratio:

$$\mathbb{Y}_r^{enh} = (1 - c) Y_r \begin{pmatrix} 1 \\ 1 \\ 1 \end{pmatrix} + c \mathbb{Y}_r, \quad (19)$$

where parameter  $c$  depends on the radiologist's personal preference:

$$c = \begin{cases} 0.15 & \text{light} \\ 0.3 & \text{medium} \\ 0.6 & \text{heavy} \\ 1.0 & \text{full.} \end{cases} \quad (20)$$

We experimentally set the  $c$  parameter (20) values from our visual evaluation experiments.

### 3 Compared methods

For comparison, we have implemented four state-of-the-art methods for mammogram image enhancement [1, 13, 19, 23]. These methods enhance mammograms in the grayscale format. We are not aware of any other mammogram enhancement method producing results in color.

#### 3.1 Matting-based enhancement

This enhancement method by Wang et al. [23] is based on image matting. The method sees the mammographic images ( $Y$ ) as a superposition of adipose tissue ( $B$ ), which forms most in the background of the image, and the mammary

glands and other breast structures that the radiologists need to focus on, denoted by ( $G$ ):

$$Y = Gc + B(1 - c). \quad (21)$$

The method thus obtains the enhanced image by subtracting the tissue-based background from the original, superposed image. To do this, the background ( $B$ ) has first to be estimated for each pixel, along with the opacity alpha value indicating the factor of a linear combination with the rest of the image ( $c$ ). The background is constant across the image chosen so that approximately 85% of pixels in the breast area of the image have lower gray-level value.

#### 3.2 Nonlinear unsharp masking

Panetta et al. [13] introduced a method for mammogram enhancement based on combining nonlinear unsharp masking (NLUM) with nonlinear filtering. Several distinct filters are used in this method. The overall nonlinear filtering operator fuses both the original and the enhanced mammogram data within a  $3 \times 3$  window. High frequencies of the signal are emphasized by either subtracting a low-pass-filtered signal from its original or adding a scaled high-frequency factor to the measured original. The method's eight parameters are optimized with a proposed second-derivative-like measure of enhancement (SDME) [13].

#### 3.3 Direct contrast enhancement

Tang et al. [19] developed an enhancement method based on wavelet transformation. It transforms the mammogram image into a multi-level 2D wavelet space. Directional contrast at each level of the wavelet transformation is estimated; namely, the three high-pass components are divided, each by its low-pass part. The contrast estimate is then multiplied by a constant contrast enhancement factor  $\lambda$ . The enhanced image is acquired by running the inverse wavelet transform one level at a time. To make up for the contrast enhancement changes, the high-pass components are re-multiplied by the newly computed low-pass component in each iteration until the whole inverse is achieved. This also allows the method to enhance the image's contrast without introducing excessive additional noise.

#### 3.4 Nonlinear polynomial filters

Bhateja et al. [1] have published a method based on the nonlinear polynomial filtering framework based on quadratic Volterra filters for contrast and edge enhancement of mammographic images. The method performs both low-pass and high-pass filtering of the image and combines the output in one contrast- and edge-enhanced result.

## 4 Results

Our method was tested on mammograms from the INbreast database [12] and mammograms acquired by the digital mammograph Senographe 2000 D. The Senographe 2000 D produces high-resolution (100 microns)  $1920 \times 2300$  images with 14-bit pixel quantization.

The INbreast database is a database of digital mammographic images acquired at a breast center of the Hospital de São João, Breast Centre University Hospital, Porto, Portugal. INbreast contains 115 cases (410 images), out of which 90 examples are from women with both breasts (four images per case) and 25 cases are from mastectomy patients (two images per case). It includes various types of lesions (masses, calcifications, asymmetries and distortions). There are 67 images containing no suspicious regions. The database contains ground-truth contours made by specialists.

### 4.1 Contrast measures

We have implemented three different contrast measures to evaluate our results. The local contrast is computed using a slightly modified second-derivative-like measure of enhancement (SDME) proposed by Panetta [13], Border contrast by Erdem et al. [4] and the weighted-level framework with retinal-like subsampling contrast (Wlf(Rsc)) proposed by Simone et al. [18]. A detailed survey of 11 local image contrast measures is presented in [15] where they are mutually compared, and their robustness to different types of image degradation is analyzed.

#### 4.1.1 Modifying contrast measures for regions of interest

Measuring the contrast for local abnormality enhancement is somewhat dubious since ideally, we want to lower the contrast of healthy tissue as much as possible and only raise the contrast of the abnormalities. Denoting  $A$  as an abnormality and  $B$  as breast, we propose the following modification to contrast measures to make them suitable for measuring the contrast of the regions of interest:

$$\text{Contrast Factor} = \frac{\text{Contrast}(A)}{\text{Contrast}(B \setminus A)} \tag{22}$$

This way we can compute the factor by which the contrast at the abnormality is higher (or lower) than the contrast in the rest of the breast image. The same equation can be directly applied to global contrast measures like the SDME. For local contrast measures, which give a local contrast value for each pixel (denoted  $L(r_1, r_2)$ , where  $r_1, r_2$  are spatial indices), such as the Wlf(Rsc), we sum the values for each pixel beforehand and take their mean value:

$$\text{Contrast Factor} = \frac{|B \setminus A|}{|A|} \frac{\sum_{r_1, r_2 \in A} L(r_1, r_2)}{\sum_{r_1, r_2 \in (B \setminus A)} L(r_1, r_2)} \tag{23}$$

#### 4.1.2 Second-derivative-like measure of enhancement

The contrast measure computes the mean contrast of the image divided into  $k_1 \times k_2$  windows:

$$\begin{aligned} SDME &= -\frac{1}{k_1 k_2} \sum_{k=1}^{k_1} \sum_{l=1}^{k_2} 20 \ln \left| \frac{Y_{\max, k, l} - 2Y_{\text{center}, k, l} + Y_{\min, k, l}}{Y_{\max, k, l} + 2Y_{\text{center}, k, l} + Y_{\min, k, l}} \right|, \end{aligned} \tag{24}$$

where  $Y_{\max, k, l}$  denotes the maximum value in window  $k, l$ , while  $Y_{\min, k, l}$  denotes the minimum value in window  $k, l$  and  $Y_{\text{center}, k, l}$  denotes the center pixel value in window  $k, l$ . We set  $k_1$  and  $k_2$  in our experiments so that the windows are of the size  $5 \times 5$  px.

#### 4.1.3 Border contrast

The contrast measure computes the mean difference of pixel values along the border of a region of interest. For each region of interest  $R_i$  and each border pixel  $b(R_i)$ , it computes the mean pixel values  $\mu_{\text{in}_j}$  and  $\mu_{\text{out}_j}$  of small windows next to the border inside and outside of the desired region of interest, normalized by the image's maximum pixel value  $Y_{\max}$ . The value of  $n_s$  is a normalization factor denoting the number of spectral bands of the image so that grayscale images can be compared with multispectral ones.

$$\text{Border} = \frac{100}{Y_{\max} \sqrt{n_s}} \sum_i |b(R_i)| \sum_i \sum_{j \in b(R_i)} \|\mu_{\text{in}_j} - \mu_{\text{out}_j}\|. \tag{25}$$

Here, we have selected a window of size  $3 \times 3$  px, with the window's center 5 px distant from the border.

#### 4.1.4 Weighted-level framework

The weighted-level framework with retinal-like subsampling contrast (Wlf(Rsc)) method works in the CIELAB color space averaging the values of the actual bands. This method is based on the idea of the difference of Gaussians combined with a Gaussian pyramid.

$$\begin{aligned} Wlf_{Rsc} &= \frac{1}{N_l} \sum_{l=1}^{N_l} \lambda_l \bar{c}_l \\ \bar{c}_l &= \sum_{r_1} \sum_{r_2} c_{r_1, r_2} \end{aligned}$$

$$\begin{aligned}
c_{r_1, r_2} &= \sum_{i=3\rho_c}^{3\rho_c} \sum_{j=3\rho_c}^{3\rho_c} \text{Cen}(i, j) Y_{r_1+i, r_2+j} \\
&\quad - \sum_{i=3\rho_s}^{3\rho_s} \sum_{j=3\rho_s}^{3\rho_s} \text{Sur}(i, j) Y_{r_1+i, r_2+j} \\
\text{Cen}(i, j) &= \exp \left[ -\left(\frac{i}{\rho_c}\right)^2 - \left(\frac{j}{\rho_c}\right)^2 \right] \\
\text{Sur}(i, j) &= 0.85 \left(\frac{\rho_c}{\rho_s}\right)^2 \exp \left[ -\left(\frac{i}{\rho_s}\right)^2 - \left(\frac{j}{\rho_s}\right)^2 \right] \quad (26)
\end{aligned}$$

where  $N_l$  is the number of levels in the Gaussian pyramid,  $\bar{c}_l$  is the mean contrast at the subsampled level  $l$ ,  $i$  is the index of the color channel,  $\lambda_l$  is the weight of level  $l$ ,  $\rho_c$  (or  $\rho_s$ ) denotes the radius for the centered (or surrounding) Gaussian, respectively, and  $r_1, r_2$  are spatial indices.

For the purpose of evaluation, we choose the values of free parameters according to [18], namely  $\rho_c = 1$ ,  $\rho_s = 2$  and  $\lambda_l$ , as the variance of pixel values in each channel at level  $l$ .

## 4.2 Numerical contrast results

We present the mean results of the individual contrast measures applied to all the images in the INbreast database in Table 1. The contrast measures were computed on images subsampled to 1024 px height, keeping aspect ratio, and with the region of interest overlapping at 20 px to cover the context of the computed ROI. The SDME contrast measure is computed on grayscale images, whereas the border contrast and Wlf(Rsc) are computed in the CIELAB color space. Furthermore, we distinguish between the contrasts computed for different types of ROIs: masses, calcifications and all ROIs together. The best results for each set are printed in boldface and the presented method's outputs in italics.

## 5 Discussion

### 5.1 Numerical evaluation

The three contrast measures exhibit different sensitivities, depending on the types of information measured. The most consistent results can be seen in the Wlf(Rsc) contrast, which confirms our assumption that the prediction probability-based enhancement is more suitable for enhancing masses while the prediction error and combined methods are more suitable for calcifications. The combined method is more sensitive to lesions than the prediction error-based method. Since calcifications cover most of the ROIs taken from the INbreast database, the overall results (bottom part of Table 1) are more biased toward the calcification-focused approaches.

**Table 1** Contrast comparison

Method	Wlf (Rsc)	SDME	Border
<i>Masses</i>			
Bhateja [1]	0.96	0.99	2.84
Combined (18)	1.02	1.00	7.96
Original	0.94	0.99	1.29
Panetta [13]	0.94	0.95	1.89
Pred. errors (17)	0.88	<b>1.01</b>	7.53
Pred. probabs. (16)	<b>1.65</b>	0.98	<b>10.8</b>
Tang [19]	0.76	1.00	2.35
Wang [23]	1.02	0.82	6.26
<i>Calcifications</i>			
Bhateja	0.98	0.98	2.90
Combined	<b>1.79</b>	<b>1.00</b>	7.76
Original	0.97	0.99	1.35
Panetta	0.98	0.97	2.20
Pred. errors	1.72	<b>1.00</b>	7.49
Pred. probabs.	1.05	0.99	<b>10.8</b>
Tang	0.82	0.99	2.16
Wang	1.03	0.90	6.39
<i>All ROIs together</i>			
Bhateja	0.97	0.99	2.87
Combined	<b>1.78</b>	<b>1.00</b>	7.78
Original	0.97	0.99	1.33
Panetta	0.97	0.96	2.13
Pred. errors	1.64	<b>1.00</b>	7.42
Pred. probabs.	1.27	0.99	<b>10.7</b>
Tang	0.81	0.99	2.15
Wang	1.02	0.88	6.26

The contrast criteria suggest that our method significantly outperforms the compared alternatives even in grayscale images. The alternative methods may occasionally exhibit contrast values even lower than those encountered in the original images.

### 5.2 Visual evaluation

Figure 2 shows an example of a mediolateral oblique (MLO) mammogram with a low-contrast lesion and a big calcification. The lesion is better visible in the prediction probability-based image  $\mathbb{Y}^b$  (16), which on the other hand almost does not show the calcification, whereas the calcification is brightly highlighted in the prediction error-based image  $\mathbb{Y}^s$  (17). The combined image  $\mathbb{Y}^m$  (18) shows both abnormalities acceptably. Figure 3 shows another MLO mammogram with an elliptical lesion near its edge. The lesion is visible with equal ease in all three enhanced images. In Fig. 4, there is a very small malignancy in a craniocaudal (CC) mammogram. Because of its size and relatively low contrast in compari-

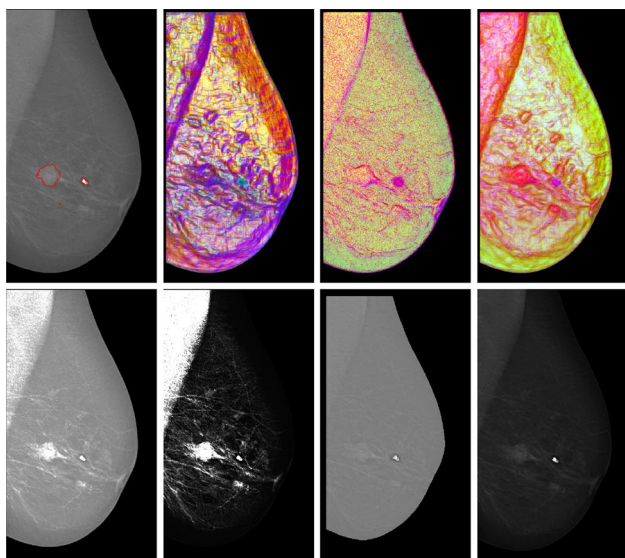


**Fig. 2** Enhanced example with a lesion and a big calcification. Top row from left to right: original with ground truth, enhancement based on prediction probabilities, enhancement based on prediction errors and combined enhancement. Bottom row from left to right: comparison methods by [13], [23], [19] and [1]

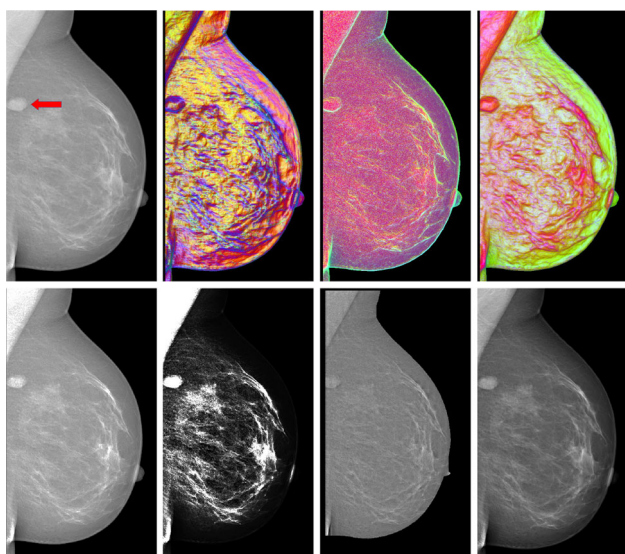


**Fig. 3** Examples of enhancement. Top row from left to right: original with ground truth, enhancement based on prediction probabilities, enhancement based on prediction errors and combined enhancement. Bottom row from left to right: comparison methods by [13], [23], [19] and [1]

son with its surroundings, it is not very visible in either the prediction probability-based enhancement ( $\mathbb{Y}^s$ ) or the prediction error-based one ( $\mathbb{Y}^e$ ). The combined view  $\mathbb{Y}^m$ , however, shows it as a bright red circle.

There are several microcalcifications in the CC mammogram in Fig. 5. They are marked as thick blue dots in the prediction error-based image  $\mathbb{Y}^e$  and as rather bluish dots in

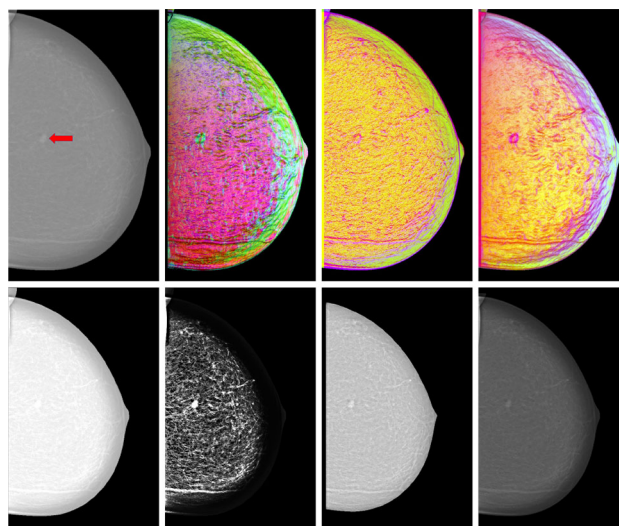


**Fig. 4** Enhanced example with a dimly visible cancer. Top row from left to right: original with ground truth, enhancement based on prediction probabilities, enhancement based on prediction errors and combined enhancement. Bottom row from left to right: comparison methods by [13], [23], [19] and [1]

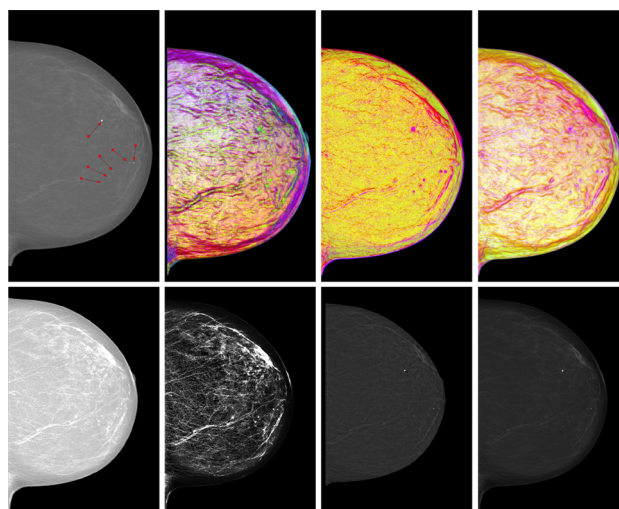


**Fig. 5** Enhanced example with several microcalcifications. Top row from left to right: original with ground truth, enhancement based on prediction probabilities, enhancement based on prediction errors and combined enhancement. Bottom row from left to right: comparison methods by [13], [23], [19] and [1]

the combined view  $\mathbb{Y}^m$ . Because of their size and character, they are omitted by the prediction probability-based image  $\mathbb{Y}^s$ .

In the bottom rows of Figs. 2, 3, 4, 5 and 6, we can see a comparison with methods by Panetta et al., Wang et al., Tang et al. and Bhateja et al. The advantage of our method is in making clearly visible contours around texture abnormalities, microcalcifications and malignant findings while keeping non-suspicious mammograms (Fig. 6) fairly homogeneous in comparison with these alternative methods.

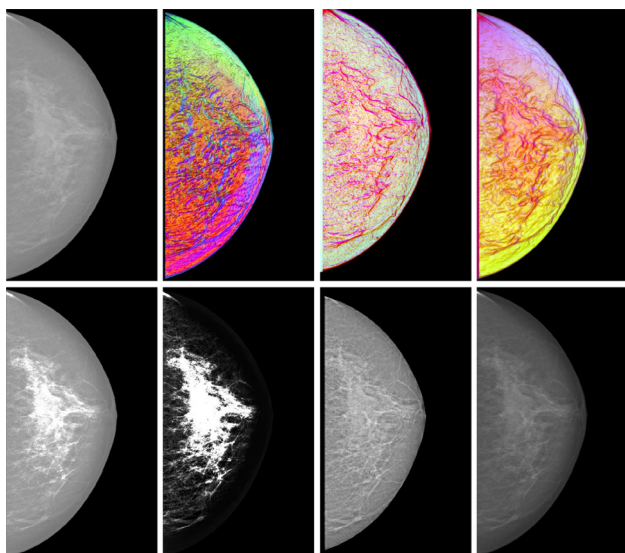


**Fig. 6** Enhanced benign example. Top row from left to right: original image, enhancement based on prediction probabilities, enhancement based on prediction errors and combined enhancement. Bottom row from left to right: comparison methods by [13], [23], [19] and [1]

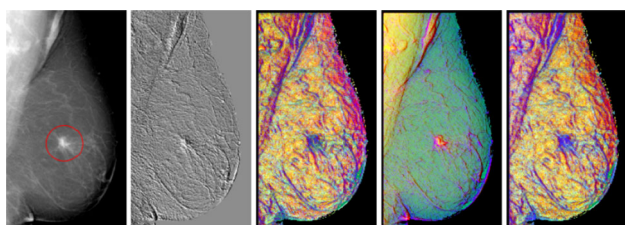


**Fig. 7** Example of the presented method compared with our previous result. Left to right: original with ground truth, enhancement by our previous method [9], enhancement based on prediction probabilities, enhancement based on prediction errors and combined enhancement

Figure 7 shows an example of enhancement in one of the digital mammograph Senographe 2000 D mammograms using the single-directional rightward 2DCAR model using our previously published method [9] compared with our new method. It is visible that the lesion and the lymph nodes are better visible in the colored images. The lesion is better visible in the prediction probability-based enhancement  $\mathbb{Y}^b$  and in the combined enhancement  $\mathbb{Y}^m$  (which is not too different from the probability-based one due to lower quality of input data), and the nodes are better visible in the prediction error-based image  $\mathbb{Y}^s$ .

The use of targeted frequency bands makes the algorithm more susceptible to abnormalities of different sizes, ranging from microcalcifications (Fig. 5) to medium-size lesions (Fig. 2) and lymph nodes. Larger lesions are enhanced with somewhat lower contrast, but since they can easily be seen with the naked eye even by untrained people, we do not see this limitation as a serious drawback.

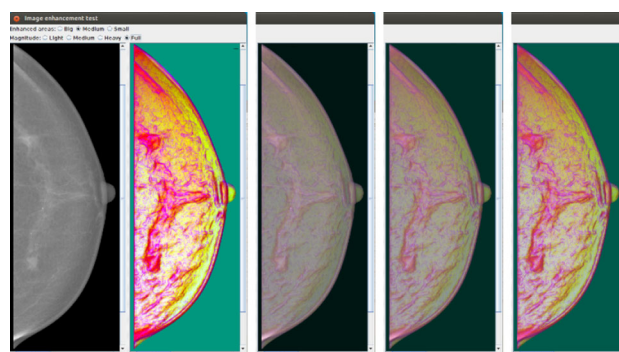


**Fig. 8** Screenshots of the radiologist validation program—test B

### 5.3 Radiologists verification

The presented method was consulted with five senior expert radiologists who focus solely on mammography. The radiologists underwent a test using a perceptual validation program working with the INbreast database images.

This program generates two types of tests: either the perceptual validation test on the original X-ray mammograms (blind test A) or the test where each window contains the X-ray measurements on the left half of the screen and its enhanced version using the presented method on the right half (enhanced test B, Fig. 8).

The radiologists were asked to click on all suspicious-looking spots in the mammogram. They could choose from the three different types ( $\mathbb{Y}^b$ ,  $\mathbb{Y}^s$  and  $\mathbb{Y}^m$ ) of enhancement combined with one of the four enhancement levels (light, medium, heavy and full) (20). All tests were performed with only a two-minute introduction without any previous schooling or trials.

Single test screens for both test types were randomly chosen from the combined INbreast database and the corresponding enhanced mammograms. The success rate of every radiologist was evaluated together with the time spent on evaluation of each spot, screen and left or right image (for test B).

Each standard test (both A and B) contains 20 different screens, i.e., 40 screens total with images of both benign and malignant instances. However, due to time constraints of the participants, test A is missing, and test B contains just 10 and 16 cases, respectively, for radiologist numbers 2 and 3. Although any more definite conclusion would need a much larger study, we believe that these results indicate the positive trend of our method. Average time per case for test B is about three times longer than for test A, which is not surprising due to the novelty of the presented method and 12 different configurations of the enhancement settings. We expect comparable times in routine usage.

The results, shown in Table 2, were comparable. At first glance, the results of test B might look a bit worse, which

**Table 2** Tests A and B

Radiologist	#ROIs	#CS	#TS	TPC (s)
<i>Test A</i>				
1	5	5	26	28
2	–	–	–	–
3	–	–	–	–
4	5	5	9	11
5	8	7	22	16
<i>Test B</i>				
1	11	11	29	63
2	5	4	9	27
3	5	5	14	138
4	4(3)	3	17	36
5	7	6	14	42

Radiologists 2 and 3 did not take test A, *CS* correctly selected, *TS* total selected, *TPC* time per case

**Table 3** Summary

Test	TP (%)	FP (%)	FN (%)	Time (s)
<i>Summary</i>				
A	94	70	5	18
B	90	65	9	62
B*	96	65	4	62

*TP* true positives, *FP* false positives, *FN* false negatives

B\* means B after discussion

would speak against the proposed enhancement method, since while the radiologists missed only one abnormality in test A, they missed two abnormalities in test B. However, the abnormality missed by radiologist No. 5 in test A was classified as BI-RADS 4c, which means higher than intermediate suspicion of malignancy, whereas the abnormalities omitted in test B were BI-RADS 2 and 3, which means benign (BI-RADS 2) and probably benign (BI-RADS 3) findings. Moreover, when we discussed the missed abnormalities with the experts after the test, we found out that radiologist No. 4 did not highlight the BI-RADS 2 finding deliberately as she found it to be a non-suspicious texture summation. Considering this, we added a third row to the summary Tab. 3 to show the corrected results. Our radiologist consultants expressed keen interest in the method and appreciated its outputs.

## 6 Conclusions

We have proposed a novel fast method with three complementary targeted outputs for completely automatic mammogram enhancement. Our method is based on the underlying two-dimensional adaptive texture model which automatically adapts to the analyzed X-ray, thus being universal

for any input without the need for further manual tuning of specific parameters. Although the algorithm uses a random-field-type model, this model is very fast thanks to efficient recursive and numerically robust model estimation, and therefore, it is much faster than the usual alternative Markov random-field models, which require an approach based on the Markov chain Monte Carlo estimation.

Our method's outputs highlight regions of interest detected as textural abnormalities. Cancerous areas typically manifest themselves in X-ray images such as textural defects. Thus, the enhanced mammograms can help radiologists to decrease their false negative evaluation rate. It has been shown that the algorithm works well both for small findings, such as microcalcifications, and for bigger lesions. In the examples, it can be seen that even barely visible abnormalities, with the same average gray level as their surroundings, are highlighted very well using our methods, and this could be of great benefit in breast cancer detection. A radiologist can choose to view either one targeted enhanced X-ray or all three enhanced alternatives.

We have compared our method with four state-of-the-art methods and visually and numerically evaluated the results. Our method shows better sensitivity for enhancing both larger and smaller abnormalities. These observations are confirmed by numerical state-of-the-art contrast criteria and also by our radiologist consultants.

**Acknowledgements** This research was supported by the Czech Science Foundation Project GAČR 19-12340S.

## References

- Bhateja, V., Misra, M., Urooj, S.: Non-linear polynomial filters for edge enhancement of mammogram lesions. *Comput. Methods Progr. Biomed.* **129**, 125–134 (2016)
- Chang, C.M., Laine, A.: Coherence of multiscale features for enhancement of digital mammograms. *IEEE Trans. Inf. Technol. Biomed.* **3**(1), 32–46 (1999)
- Dippel, S., Stahl, M., Wiemker, R., Blaffert, T.: Multiscale contrast enhancement for radiographies: Laplacian pyramid versus fast wavelet transform. *IEEE Trans. Med. Imaging* **21**(4), 343–353 (2002)
- Erdem, C.E., Sankur, B., Tekalp, A.M.: Performance measures for video object segmentation and tracking. *IEEE Trans. Image Process.* **13**(7), 937–951 (2004)
- Grim, J., Somol, P., Haindl, M., Daneš, J.: Computer-aided evaluation of screening mammograms based on local texture models. *IEEE Trans. Image Process.* **18**(4), 765–773 (2009). <https://doi.org/10.1109/TIP.2008.2011168>
- Haindl, M.: Texture synthesis. *CWI Q.* **4**(4), 305–331 (1991)
- Haindl, M.: Visual data recognition and modeling based on local markovian models. In: Florack, L., Duits, R., Jongbloed, G., Lieshout, M.C., Davies, L. (eds.) *Mathematical Methods for Signal and Image Analysis and Representation*, Computational Imaging and Vision, vol. 41, pp. 241–259. Springer, London (2012). [https://doi.org/10.1007/978-1-4471-2353-8\\_14](https://doi.org/10.1007/978-1-4471-2353-8_14)

8. Haindl, M., Mikeš, S., Scarpa, G.: Unsupervised detection of mammogram regions of interest. In: Apolloni, B., Howlett, R.J., Jain, L. (eds.) *Knowledge-Based Intelligent Information and Engineering Systems*. LNAI, vol. 4694, pp. 33–40. Springer, Berlin (2007). [https://doi.org/10.1007/978-3-540-74829-8\\_5](https://doi.org/10.1007/978-3-540-74829-8_5)
9. Haindl, M., Remeš, V.: Efficient textural model-based mammogram enhancement. In: P.P. Rodrigues, M. Pechenizkiy, J. ao Gama, R. Cruz-Correia, J. Liu, A. Traina, P. Lucas, P. Soda (eds.) *2013 IEEE 26th International Symposium on Computer-Based Medical Systems (CBMS)*, pp. 522–523. IEEE, Hoes Lane, P.O. Box 1331, Piscataway, NJ 08855-1331, USA (2013). <https://doi.org/10.1109/CBMS.2013.6627859>
10. Haindl, M., Šimberová, S.: *A Multispectral Image Line Reconstruction Method. Theory and Applications of Image Analysis*, pp. 306–315. World Scientific Publishing Co., Singapore (1992)
11. Mencattini, A., Salmeri, M., Lojacono, R., Frigerio, M., Caselli, F.: Mammographic images enhancement and denoising for breast cancer detection using dyadic wavelet processing. *IEEE Trans. Instrum. Meas.* **57**(7), 1422–1430 (2008)
12. Moreira, I.C., Amaral, I., Domingues, I., Cardoso, A., Cardoso, M.J., Cardoso, J.S.: Inbreast: toward a full-field digital mammographic database. *Acad. Radiol.* **19**(2), 236–248 (2012)
13. Panetta, K., Zhou, Y., Agaian, S., Jia, H.: Nonlinear unsharp masking for mammogram enhancement. *IEEE Trans. Inf. Technol. Biomed.* **15**(6), 918–928 (2011)
14. Qi, H., Diakides, N.A.: Thermal infrared imaging in early breast cancer detection—a survey of recent research. In: *Proceedings of the 25th Annual International Conference of the IEEE Engineering in Medicine and Biology Society*, vol. 2, pp. 1109–1112. IEEE (2003)
15. Remeš, V., Haindl, M.: Region of interest contrast measures. *Kybernetika* **54**(5), 978–990 (2018). <https://doi.org/10.14736/kyb-2018-5-0978>. <https://www.kybernetika.cz/content/2018/5/978/paper.pdf>
16. Sakellariopoulos, P., Costaridou, L., Panayiotakis, G.: A wavelet-based spatially adaptive method for mammographic contrast enhancement. *Phys. Med. Biol.* **48**(6), 787 (2003)
17. Salvado, J., Roque, B.: Detection of calcifications in digital mammograms using wavelet analysis and contrast enhancement. In: *2005 IEEE International Workshop on Intelligent Signal Processing*, pp. 200–205. IEEE (2005)
18. Simone, G., Pedersen, M., Hardeberg, J.Y.: Measuring perceptual contrast in digital images. *J. Visual Commun. Image Represent.* **23**(3), 491–506 (2012)
19. Tang, J., Liu, X., Sun, Q.: A direct image contrast enhancement algorithm in the wavelet domain for screening mammograms. *IEEE J. Sel. Top. Signal Process.* **3**(1), 74–80 (2009). <https://doi.org/10.1109/JSTSP.2008.2011108>
20. Taylor, P., Champness, J., Given-Wilson, R., Johnston, K., Potts, H.: Impact of computer-aided detection prompts on the sensitivity and specificity of screening mammography. *Health Technol. Assess.* **9**(6), 1–58 (2005)
21. Thangavel, K., Karnan, M., Sivakumar, R., Mohideen, A.: Cad system for preprocessing and enhancement of digital mammograms. *Graphics, Vision and Image Processing* pp. 55–60 (2007). <http://www.icgst.com/gvip/v7/P1150527002.html>
22. Tweed, T., Miguet, S.: Automatic detection of regions of interest in mammographies based on a combined analysis of texture and histogram. In: *2002 Proceedings of 16th International Conference on Pattern Recognition*, vol. 2, pp. 448–452. IEEE Computer Society, Los Alamitos, CA, USA (2002). <https://doi.org/10.1109/ICPR.2002.1048335>
23. Wang, H., Li, J.B., Wu, L., Gao, H.: Mammography visual enhancement in cad-based breast cancer diagnosis. *Clin. Imaging* **37**(2), 273–282 (2013)
24. Yan, Z., Zhang, Y., Liu, B., Zheng, J., Lu, L., Xie, Y., Liang, Z., Li, J.: Extracting hidden visual information from mammography images using conjugate image enhancement software. In: *2005 IEEE International Conference on, Information Acquisition*, pp. 4775–4778. IEEE Engineering in Medicine and Biology Society, IEEE (2005)

**Publisher's Note** Springer Nature remains neutral with regard to jurisdictional claims in published maps and institutional affiliations.



**Michal Haindl** graduated from the Czech Technical University (1979), Prague, received his Ph.D. from the Czechoslovak Academy of Sciences (1983), and subsequently earned the DSc degree (2001). He is the IAPR fellow, IEEE senior member, and Professor. Since 1983 he has worked on various image analysis and pattern recognition topics in the Institute of Information Theory and Automation (UTIA) of the Czechoslovak Academy of Sciences, Prague; University of Newcastle; Rutherford Appleton Laboratory; CWI, Amsterdam; and INRIA, Rocquencourt. In 1995, he rejoined UTIA where he is the Pattern Recognition Department head. He is the author of one book and about 330 research papers published in books, journals, and conference proceedings. His current research interests include random fields applications in pattern recognition and image processing.



**Václav Remeš** graduated MSc. in software systems at Faculty of Mathematics and Physics of the Charles University in Prague (2010) and received Ph.D. in pattern recognition at Faculty of Information Technology of the Czech Technical University (2018). His areas of interests include pattern recognition and texture modeling.